CHEMISTRY OF MATERIALS

pubs.acs.org/cm Article

High Voltage Mg-Ion Battery Cathode via a Solid Solution Cr−Mn Spinel Oxide

Bob Jin Kwon,* Liang Yin, Haesun Park, Prakash Parajuli, Khagesh Kumar, Sanghyeon Kim, Mengxi Yang, Megan Murphy, Peter Zapol, Chen Liao, Timothy T. Fister, Robert F. Klie, Jordi Cabana, John T. Vaughey, Saul H. Lapidus, and Baris Key*

Cite This: *Chem. Mater.* 2020, 32, 6577−6587 Read Online

ACCESS | Metrics & More | Article Recommendations | Supporting Information

ABSTRACT: Lattice Mg^{2+} in a tailored solid solution spinel, $MgCrMnO_4$, is electrochemically utilized at high Mn-redox potentials in a nonaqueous electrolyte. Complementary evidence from experimental and theoretical analyses supports bulk Mg^{2+} (de)intercalation throughout the designed oxide frame where strong electrostatic interaction between Mg^{2+} and O^{2-} exists. Mg/Mn antisite inversion in the spinel is lowered to ∼10% via postannealing at 350 °C to further improve Mg^{2+} mobility. Spinel lattice is preserved upon removal of Mg^{2+} without any phase transformations, denoting structural stability at the charged state at a high potential ∼3.0 V (vs Mg/Mg^{2+}). Clear remagnesiation upon first discharge, harvesting up to ∼180 Wh/kg at 60 °C is shown. In the remagnesiated state, insertion of Mg^{2+} into interstitial sites in the spinel is detected, possibly resulting in partial reversibility which needs to be addressed for structural stability. The observations constitute a first clear path to the development of a practical high voltage Mg-ion cathode using a spinel oxide.

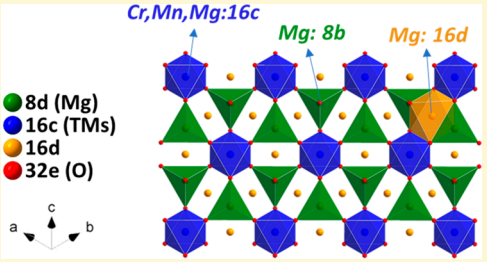

INTRODUCTION

Nonaqueous Mg-ion batteries have been considered as an alternative to Li-ion technology with the potential to deliver high energy density at low cost.[1,2] This strongly depends on the discovery of cathode materials with reversible storage capacity operating at high potentials.[3,4] However, reversible intercalation of Mg^{2+} has been achieved in a limited number of frameworks, mainly composed of soft anions, such as Mo_6X_8 (X = S, Se) and TiS_2.[5,6] These phases, while being suitable for reversibility and stability, with their low operating potentials (∼1 V vs Mg/Mg^{2+}) severely limit the energy density of the electrochemical cells highlighting the need to explore new compounds where Mg^{2+} is reversibly intercalated at high redox potentials. In theory, the potential can be raised by utilizing an oxide framework instead, while preserving structural flexibility that enables and sustains percolating pathways for Mg^{2+} migration at all states of charge.[7] However, such paths of Mg^{2+} show relatively high barriers to cation hopping in oxide lattices, due to the existence of strong electrostatic interactions between the localized charges at Mg^{2+} and O^{2-}.[7,8] Consequently, sluggish migration of Mg^{2+} has been assigned as the main cause of the poor electrochemical properties of oxide cathodes with overpotentials so large as to open up alternate pathways for electrochemical conversion and/or amorphization instead, where the oxide is reduced by losing O^{2-} rather than by intercalating Mg^{2+}.[9,10] As a result, it is necessary to design new functional oxides, which utilize facile Mg^{2+} in the lattice at high redox potentials in a nonaqueous electrolyte.

Theoretical and experimental evidence has revealed that oxide spinels constitute a possible host favorable for intercalation of multivalent cations owing to their three-dimensional pathways of migration.[8,11] The spinel structures are expected to provide feasible integration of operational potential, capacity, and cation mobility, as indicated in the theoretical predictions.[8] Feasibility of Mg^{2+} intercalation into host Mn_2O_4 was demonstrated in an aqueous electrolyte system,[12] experimentally, but the activation energy (∼0.8 eV) of Mg^{2+} migration in Mn-spinel strongly limits preferential (de)intercalation of Mg^{2+} when conjugated with a nonaqueous Mg electrolyte.[8,13] Moreover, inversion between Mg^{2+} and Mn^{2+}, by disproportionation of Mn ions,[14−16] has been observed in a $MgMn_2O_4$ spinel synthesized at high temperatures which raises a barrier of cation migration in the lattices.[13,16] As an outcome of theoretical screening on various spinels, $MgCr_2O_4$ satisfies relatively facile mobility with ∼0.6 eV of activation energy for a Mg^{2+} hop to an adjacent vacancy site, which is further estimated by density functional theory (DFT), solid-state nuclear magnetic resonance (ss-NMR), and muon-spin relaxation experiments.[16,17] However, the high redox potentials for (de)intercalation of Mg^{2+} (∼3.7 V vs Mg/Mg^{2+}) preclude the practicality of $MgCr_2O_4$ as a functional cathode

Received: May 11, 2020
Revised: July 14, 2020
Published: July 14, 2020

https://dx.doi.org/10.1021/acs.chemmater.0c01988
Chem. Mater. 2020, 32, 6577−6587

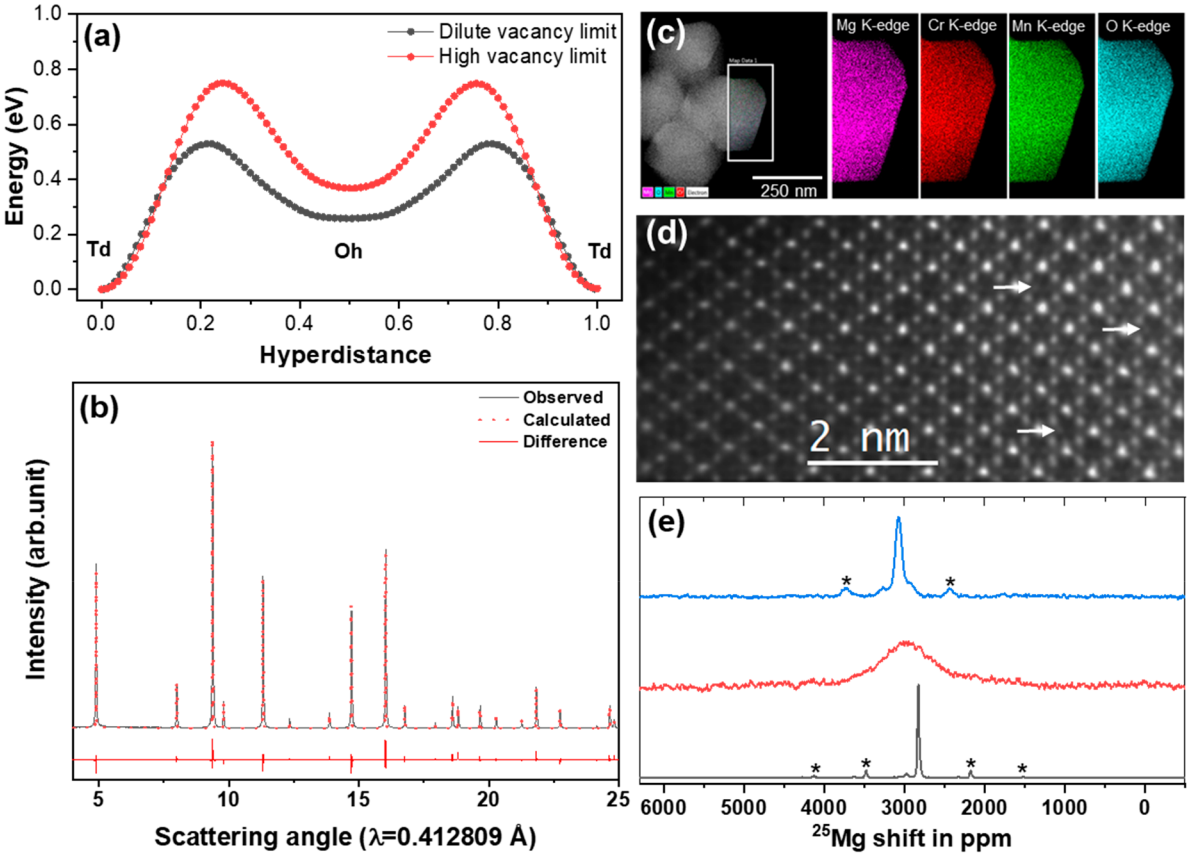

Figure 1. (a) Minimum energy pathways of Mg^{2+} migration in $MgCrMnO_4$ at the high and dilute vacancy limits. (b) Synchrotron XRD pattern, (c) STEM-EDX mapping, and (d) atomic HAADF image of $MgCrMnO_4$ along with [110] showing spinel structure. Arrows show the nonuniform intensity across the tetrahedral sites within the spinel unit. (e) Solid-state NMR spectra of $MgCr_2O_4$ (black), $MgCrMnO_4$ (red), and $MgMn_2O_4$ (blue). Asterisk marks indicate spinning sidebands.

when paired with current state-of-the-art nonaqueous Mg-ion electrolytes, limiting an upper cutoff potential to ~3.5 V (vs Mg/Mg^{2+}).[8,16] Furthermore, the instability of the oxidized state, Cr^{4+}([Ar] $3d^2$), is another challenge in utilizing Cr redox in spinel lattices, suggesting a necessity for modifying the chemistry.[16]

The intrinsic design weaknesses in a single B site Cr- or Mn-spinel for a Mg-ion cathode are alleviated by building a solid-solution $MgCrMnO_4$ where the mixed transition metal lattice provides mobility via Mg^{2+} bound by Cr^{3+} and suitable high redox potential via Mg^{2+} bound by Mn^{3+} for (de)intercalation. Our recent study on electrochemical Mg^{2+} activity in a largely $MgCrVO_4$ spinel indicates the feasibility of the design, whereas it also shows partial reversibility of intercalation due to the structural instability and surface reconstruction by removal of Mg^{2+}.[18] In this work, a bulk Mg^{2+} activity with notable reversibility is clearly demonstrated by using a tailored single cubic phase of $MgCrMnO_4$ spinel in the electrochemical cells, conjugated with a thermally and anodically stable Mg electrolyte.[19] The mechanisms of the (de)intercalation reaction were supported by the combination of experimental and theoretical evidence with consistency. The structures as a response to Mg^{2+} (de)intercalation were examined by X-ray diffraction, microscopic, and spectroscopic characterization experiments at key states of charge. Significant structural and electronic evolutions as a response to Mg^{2+} reactions were observed in the bulk characterization techniques. It is worth noting that the clear reversible (de)intercalation of Mg^{2+} in spinel oxides has not been achieved so far in nonaqueous electrolytes. These observations of clear bulk Mg^{2+} activity in a Mg-ion cell constitute a fundamental step forward for an oxide spinel to reversibly intercalate Mg^{2+} in a nonaqueous Mg electrolyte through solid-state chemistry design, deepening our understanding on the chemistry of multivalent intercalation and reach a critical milestone in the long quest toward a high energy multivalent ion battery.

RESULTS AND DISCUSSION

The migration barrier of Mg^{2+} in the $MgCrMnO_4$ lattice was predicted by first-principles calculations at the DFT+U level of theory in both dilute and high vacancy limits (Figure 1a). The Mg^{2+} in the spinel lattices (T_d−O_h−T_d) migrates through the triangle face shared between the stable and intermediate sites, showing a hill-shaped energy profile.[16,17] The activation energy of migration reflects a feasible reactivity of Mg^{2+} at the initial and final states upon demagnesiation, utilized by (de)intercalation. The estimated barriers for a Mg^{2+} hop in the Cr−Mn spinel frame were 0.53 eV for dilute vacancy and 0.75 eV for high vacancy limits, similar to the $MgCr_2O_4$ single B-site spinel, currently known as a framework to provide the most facile Mg^{2+} among oxide spinels (Figure S1 of the Supporting Information, SI). This implies that the degree of Mg^{2+} mobility is not impeded by the introduction of Mn into a spinel in the form of solid-solution, supporting our assumption in designing a functional

https://dx.doi.org/10.1021/acs.chemmater.0c01988
Chem. Mater. 2020, 32, 6577−6587

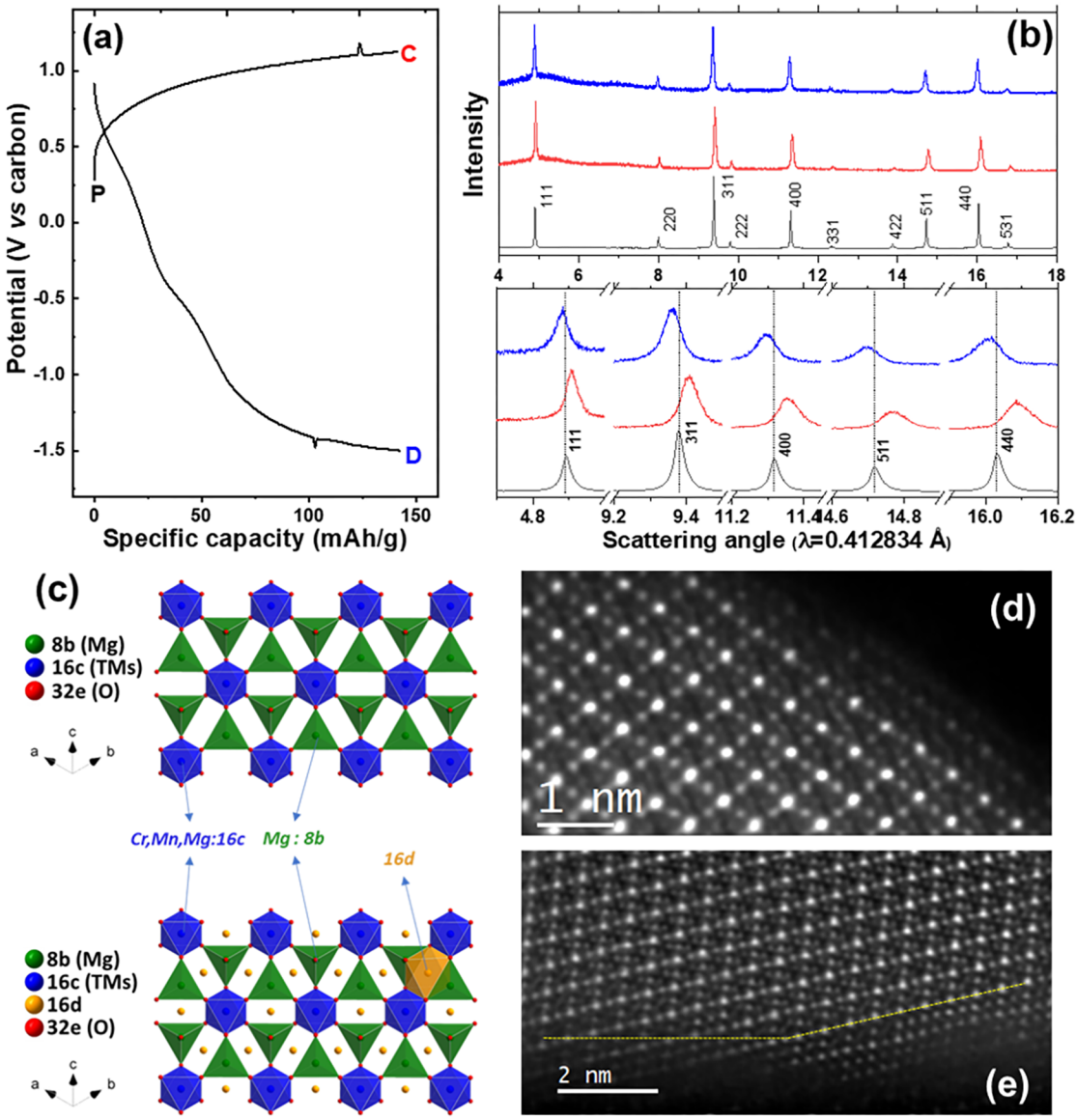

Figure 2. (a) Representative potential versus capacity profile of $MgCrMnO_4$ measured in a coin cell at 95 °C paired with a carbon counter electrode in $Mg(TPFA)_2$ electrolyte. (b) Synchrotron XRD patterns of the corresponding pristine (black), charged (red), and discharged (blue) electrode powders in wide and zoom-in angles. (c) Schematic description of two distinct Mg^{2+} occupancies in the remagnesiated spinel (TMs at 16c site indicate Cr or Mn or Mg in the spinel). HAADF-STEM images of (d) charged and (e) discharged $MgCrMnO_4$. The collected images were filtered. Charged particle shows the spinel structure across the surface and bulk, whereas rock-salt phase is detected at the surface of the discharged particle.

cathode. The target compound, nanocrystalline $MgCrMnO_4$, was synthesized via an aqueous sol−gel route followed by annealing at a controlled temperature (700 °C) to facilitate transition metal mixing while preserving nanoscale particles. The diffraction of pristine $MgCrMnO_4$ (Figure 1b) indicated a cubic spinel with a parameter of 8.3714(6) Å while presenting no discernible secondary phases or unreacted byproducts. It is worth noting that a cubic symmetry of the spinel with a long-range of order with the existence of Jahn−Teller active Mn^{3+}, could be explained by the high preference of octahedral Cr^{3+} occupancy, possibly suppressing a tetragonal distortion in the assorted lattices. Inversion of Mg/Mn was observed in the Rietveld refinement analysis, with a degree of inversion ($\lambda \approx 0.16$) being attained while presumably, the disproportionation of Mn^{3+} took place simultaneously ($2Mn^{3+}[O_h] \rightarrow Mn^{2+}[T_d] + Mn^{4+}[O_h]$).[14,20] This thermodynamically favorable cation-mixing originates from an increase of configurational entropy during high-temperature annealing.[14] For 0.16 inversion, the structural configuration of the spinel could be expressed by $(Mg_{0.84}Mn^{2+}_{0.16})^{Td}[Mg_{0.16}Cr^{3+}_{1.00}Mn^{3+}_{0.68}Mn^{4+}_{0.16}]^{Oh}O_4$. The inversion not only raises the activation barrier of Mg^{2+} in the lattice but also reduces the number of available redox-active Mn^{3+} at octahedral sites, resulting in a reduction of electrochemically utilizable lattice Mg^{2+}.[16] In $MgCrMnO_4$, preferential occupancy of octahedral Cr^{3+} with a d^3 electronic configuration[21,22] mitigates the ratio of antisite disorder in comparison to tetragonal $MgMn_2O_4$, a single B-site Mn spinel with $\lambda \approx 0.4$,[23] corresponding to an increase of Mg^{2+} percolation pathways upon electrochemical reactions.[16]

The elemental distribution and concentration of pristine $MgCrMnO_4$ were characterized by STEM-EDX mapping (Figure 1c). We found that magnesium, chromium, and

https://dx.doi.org/10.1021/acs.chemmater.0c01988
Chem. Mater. 2020, 32, 6577−6587

manganese are homogeneously distributed with a stoichiometric ratio throughout the nanocrystalline particles, consistent with a solid solution lattice (Figure S2). The average particle size was measured to be ∼50 nm using numerous particles imaged in TEM (Figure S3) which is also similar to the value of ∼55 nm estimated from Rietveld refinement. Atomic-resolution images of $MgCrMnO_4$ were acquired using high-angle annular dark-field imaging in an aberration-corrected scanning transmission electron microscopy (STEM) (Figure 1d). The crystalline spinel lattice was observed in both the bulk and surface regions of the particles without any secondary phases or surface layers (Figures 1d and S4). The difference in image contrast at two tetrahedral sites along the [110] direction was found as indicated by the arrows in Figure 1d, which is attributed to the presence of Mg/Mn inversion, consistent with diffraction analysis. The nature of the Mg^{2+} local environments in the spinel lattice was studied by solid-state Mg NMR (Figure 1e). The spectra provide Fermi contact shifts of Mg^{2+} depending on the ensemble of first and second coordination shells Mg−O−Cr/Mn connectivity in the lattice due to the presence of paramagnetic centers at Cr^{3+} and Mn^{3+} (also $Mn^{2+/4+}$) generating unique spectroscopic signatures for lattice Mg^{2+} environments alone.[18,24] The spectra of pristine $MgCrMnO_4$ showed a single broad feature with a center of mass at ∼2945 ppm (Figure 1e).[16,24] Appearing exactly halfway between the sharp resonances due to Mg^{2+} in $MgCr_2O_4$ (∼2820 ppm) and $MgMn_2O_4$ (∼3070 ppm),[24] the broad Gaussian single peak consistent with random (solid-solution) distribution of Mg/Cr−Mn in the lattice.[18] Other compositions with higher and lower Cr:Mn ratios have been successfully synthesized and will be the focus of future fundamental and applied studies, respectively. Moreover, no other distinct paramagnetic resonances from contacts between Mg^{2+} and single Cr^{3+} or Mn^{3+} was detected, indicating no presence of locally segregated clusters. While the presence of $Mn^{2+/4+}$ contributes to additional Gaussian broadening, it does not change the solid-solution assignment. The peak profile was consistent with ss-NMR[25] studies of oxides with random distribution of transition metal in layered lattices such as $Li[Ni_xMn_xCo_{(1-2x)}]O_2$ ($x = 1/3$) or in $MgMnO_2$ rock-salt lattices with random Mg and Mn ordering.[25,26]

The electrochemical properties were measured at 95 °C in a Mg half-cell consisting of an activated carbon counter electrode and spinel $MgCrMnO_4$ working electrode with a $Mg(TPFA)_2$ electrolyte dissolved in triglyme which has shown sufficient thermal and anodic stability[19] for high-temperature electrochemistry (Figure 2a). The primary function of the high surface area hard carbon is to give rise to sufficient double layer of charges to match the charge needed to cycle the cathode short-term, the capacity being completely capacitative.[27] The cell was galvanostatically charged up to the potential at a rate of C/50 where half of the theoretical capacity (∼140 mAh/g) was delivered. Then, it was discharged to −1.5 V at a constant current (C/50) until the same amount of charges was achieved. The cutoff potential corresponded to only utilization of redox $Mn^{3+/4+}$ from a theoretical standpoint, owing to the high potential of oxidation at $Cr^{3+/4+}$ in the spinel.[16,17] The conditions for the measurement aimed at investigation of behaviors of Mg^{2+} intercalation when the same amount of charges were electrochemically de- and reinserted in the oxide. The anodic reaction proceeded from ∼0.7 V (vs carbon) and a specific capacity of ∼140 mAh/g was reached up to ∼1.1 V, the reaction being centered at ∼1.0 V of a relatively constant potential (vs carbon). The Mg^{2+} content change upon demagnesiation was measured by SEM-EDX over different large areas of the electrode (Figure S5), showing a range of 0.24−0.36 mol of deintercalated Mg^{2+} (vs mol of Cr + Mn), different from 0.5 mol of Mg^{2+} equivalents reacting per mole of host based on a theoretical formula of $MgCrMnO_4$. The mismatch could be explained by the presence of antisite disorder by Mg/Mn inversion, which reduces redox-active Mn^{3+} at octahedral sites to 0.68 mol, which corresponds to 0.34 mol of utilizable Mg^{2+} and ∼95 mAh/g of actual capacity stored. Upon subsequent discharging, the profile was overall sloping with a discharge capacity of ∼140 mAh/g, achieved at −1.5 V (vs carbon), showing dominant overpotentials (Figure 2a).

Synchrotron X-ray diffraction was measured from the same harvested electrodes to gain insight into the structural evolution as a response to electrochemical Mg^{2+} reactions (Figure 2b). Diffraction of the charged electrode showed a distinct shift of peaks to higher angles in all planes of the cubic lattice as compared to the pristine, indicating a decrease of the unit cell volume in the spinel (Table 1). The lattice parameter of the pristine cubic spinel, 8.3714(6) Å, was significantly contracted to 8.3482(2) Å in the demagnesiated oxide, while no formation of secondary phase(s) via conversion reactions were detected. A visible decrease in the ratio of intensities between (111) and (311) reflections was observed, correlating to the decrease in occupancy of tetrahedral Mg^{2+}, distorting the cubic spinel (Figure S6) consistent with demagnesiation in spinels.[16] To estimate the maximal level of deintercalation from the pristine lattice, the spinel was charged up to ∼1.2 V (vs carbon) corresponding to ∼255 mAh/g (Figure S7). No further decrease in lattice parameter was observed in diffraction, revealing the apparent amount of electrochemically utilizable Mg^{2+} in the range of 0.25 to 0.35 mol (elemental composition from SEM-EDX) consistent with 0.34 mol of the theoretical value. This is also consistent with the initial assumption that Mn is a main/sole redox-participating center within the applied potential window. For the lattice charged up to 1.1 V, upon discharge with ∼140 mAh/g of capacity, diffraction peaks were reverted to lower angles consistent with remagnesiation and reversible intercalation behavior. Interestingly the peak positions move further past the pristine, due to an additional increase of lattice volume (Figure 2b). The lattice parameter of the discharged oxide was 8.3928(2) Å (Table 1), being larger than the pristine, suggesting overmagnesiation which was studied in further detail below. The broad features of peaks in the nanocrystalline oxide synthesized at 700 °C (∼50 nm, Figure S3) limited an accurate refinement of diffraction data for occupancy of reintercalated Mg^{2+} in the lattice. Consequently, larger particles (∼270 nm, Figure S8) with crystallographic long-range ordering for comparison were synthesized at a higher 950 °C which provides more suitable diffraction data and in turn crystallographic information (Figure S9). A reliable dissimilarity was a particle dimension while structural properties, such as phase purity and a degree of inversion were nearly identical (Figure S9). Larger

Table 1. Lattice Parameters and Cell Volumes of Pristine, Charged and Discharged Cubic Spinel $MgCrMnO_4$ Estimated by the Refinement of XRD Patterns in Figure 2b

state of charge	*a* parameter (Å)	cell volume (Å^3)
pristine	*8.3714(6)*	*586.68(3)*
charged	*8.3482(2)*	*581.82(4)*
discharged	*8.3928(2)*	*591.18(5)*

https://dx.doi.org/10.1021/acs.chemmater.0c01988
Chem. Mater. 2020, 32, 6577−6587

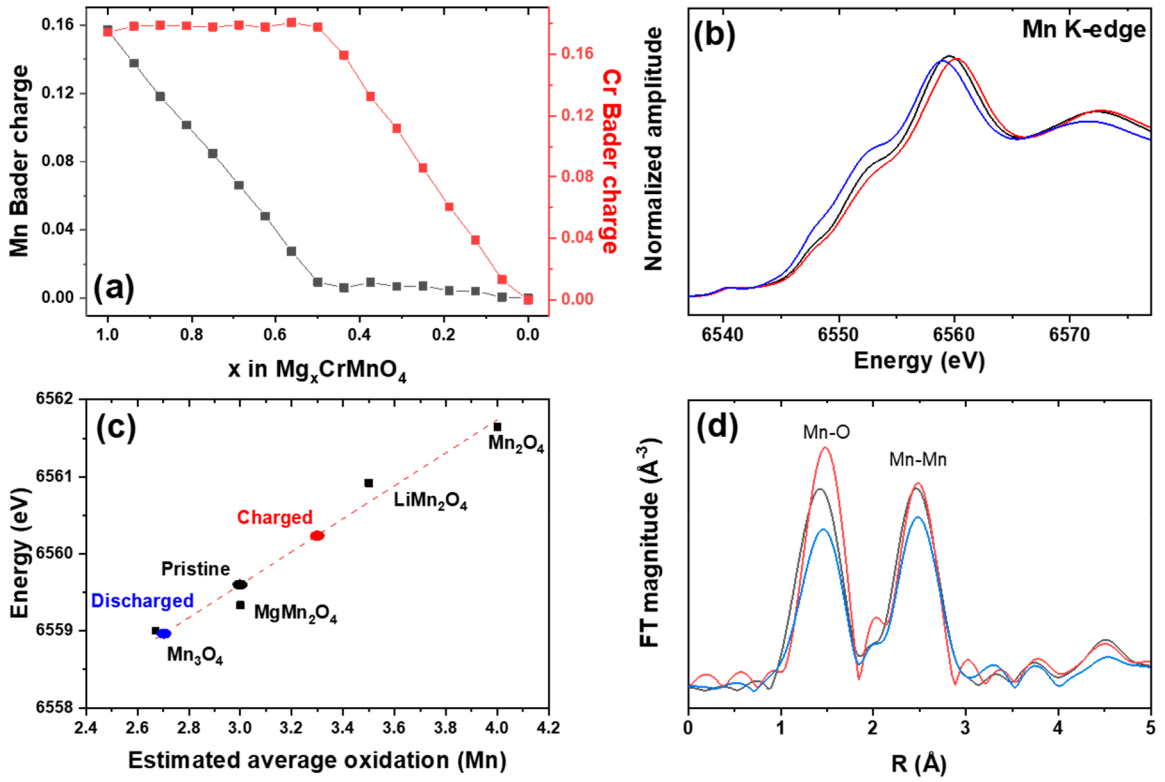

Figure 3. (a) Average Bader charges on Mn (black) and Cr (red) sites in Mg_xCrMnO_4 structures ($1 \geq x \geq 0$). Bader charges in Mn and Cr spinels are given for comparison. (b) Mn K-edge spectra of pristine (black), charged (red), and discharged (blue) electrodes. (c) The formal valence state of Mn in the samples interpolated from the position of the Mn K-edge onset in the standard spinels. (d) Extended X-ray absorption fine structure of pristine (black), charged (red), and discharged (blue) spinel $MgCrMnO_4$.

particles induced an increase of overpotentials in the electrochemical response compared to the nanocrystalline spinel prepared at 700 °C (Figure S9a). A similar degree of the shift to higher angles, with lattice contraction (8.3554 Å) was observed upon demagnesiation. Remagnesiation, interestingly, showed two clearly separate cubic spinel phases with lattice parameters of 8.3811 and 8.4185 Å (Figure S9b). As indicated in the refinement of the remagnesiated state (Figure S10), the reintercalated Mg^{2+} occupied mainly two lattice positions, a main tetrahedral 8b and interstitial octahedral 16d site which correlates closely to the trends observed in the diffraction of the smaller nanocrystals which have significant peak broadening masking these details (Figure 2c).

Local structures along the direction at different states of charge were directly visualized by atomic-resolution imaging in STEM (Figure 2d,e). In the demagnesiated nanocrystalline oxide, the spinel lattice was preserved in both the bulk and the surface regions, indicating no structural reformation on the surface by removal of Mg^{2+}, which would be a detrimental phenomenon previously observed.[18,28,29] Moreover, electron energy-loss spectroscopy (EELS) of the Mn L-edges shows the changes in the Mn valence state as a response to the Mg^{2+} deintercalation while preserving the spinel lattice (Figure S11).[30] Upon demagnesiation, the position shifts of the Mn L_3 peak by ∼1.2 eV to higher energy indicated oxidation of Mn in the spinel lattices along with a decrease in the ratio of L_3/L_2 intensity (3.37 → 2.03).[31] Moreover, the multiple empty tetrahedral sites were now visible in the atomic-resolution STEM image in demagnesiated particles (Figure 2d). Therefore, the atomic-resolution characterization confirmed the deintercalation of Mg^{2+} from the spinel lattice without phase transition in either the bulk and surface, emphasizing its phase stability at the charged state which is distinct to single B-site spinels.[16,18,29] However, the discharged oxide showed the presence of rock-salt surface layers with a thickness of ∼2 nm (Figure 2e). This observation suggests a transition from spinel to rock-salt on the surface by Mg^{2+} occupying empty octahedral sites in the spinel structure.[32] Furthermore, the concentration of Mg^{2+} in the discharged electrode was measured by STEM-EDX elemental mapping (Figure S12). We find an average atomic ratio of Mg/(Cr + Mn) in multiple areas of discharged particles of ∼0.58 (Figure S12), suggesting a comparison of approximately $Mg_{1.16}CrMnO_4$. The mechanism of Mg^{2+} intercalation suggests the importance of further optimizing the potential window so as to avoid the formation of rock-salt oxide which presumably can act as a blocking layer and limit reversibility.

Changes in average Bader charges on each species of transition metal ions versus Mg^{2+} content in the mixed spinel are shown in Figure 3a. Although a Bader charge typically is much smaller than the formal oxidation state, it is correlated with the latter and provides a reliable measure of oxidation state change.[33] Fully magnesiated, $MgCrMnO_4$, showed Cr Bader charge of 1.82e and Mn Bader charge of 1.76e, comparable to 1.83e and 1.72e charges in $MgCr_2O_4$ and $MgMn_2O_4$, respectively, and correspond to formal oxidation states of Cr^{3+} and Mn^{3+}. Upon charging, the average charge on Cr ions remains practically the same up to Mg^{2+} content of $x = 0.5$, whereas the average charge on Mn increases linearly with the decrease in Mg^{2+} content and reaches 1.93e, which is the same value as in Mn_2O_4, and corresponds to the formal oxidation state of Mn^{4+}. Therefore, we conclude that extraction of up to half of Mg^{2+} does not change Cr oxidation state, but results in oxidation

https://dx.doi.org/10.1021/acs.chemmater.0c01988
Chem. Mater. 2020, 32, 6577−6587

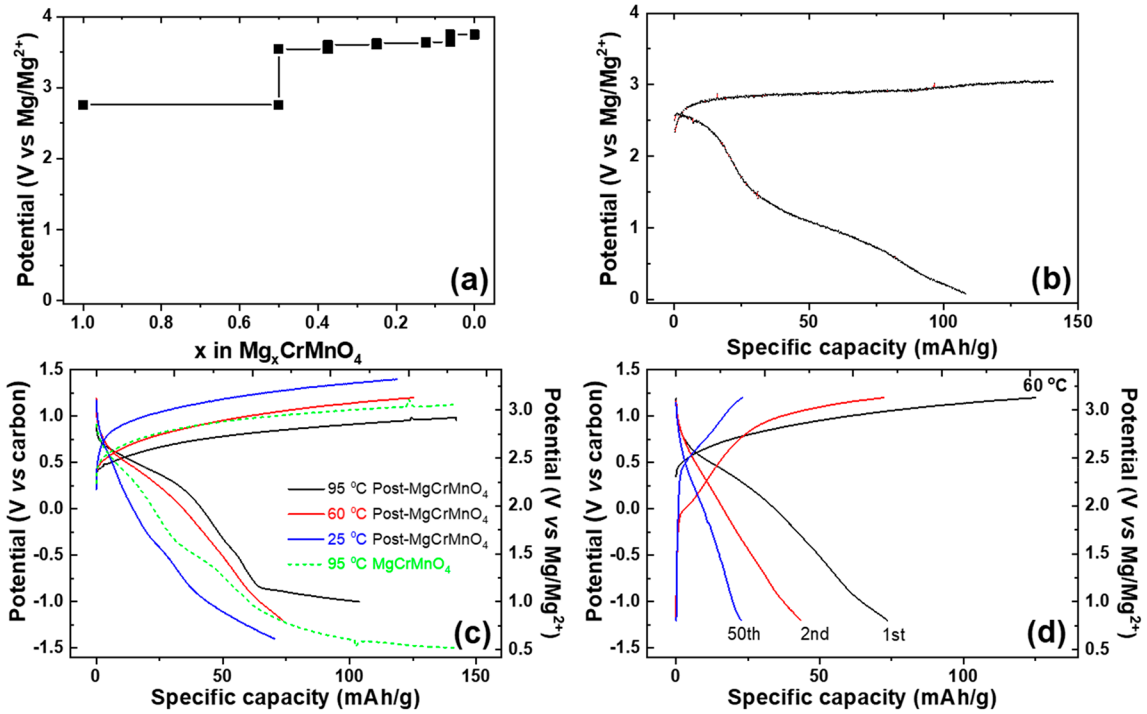

Figure 4. (a) Average potential curves in Mg_xCrMnO_4 ($1 \geq x \geq 0$), estimated by using the lowest formation energy structures across Mg concentration. (b) Representative potential versus capacity profile of $MgCrMnO_4$, paired with a Mg foil anode at 95 °C. Representative potential versus capacity profiles of post-$MgCrMnO_4$ (solid line) and $MgCrMnO_4$ (dash line) at (c) variable temperatures and (d) the different number of cycles at 60 °C when paired with a carbon counter electrode.

of Mn, because of its higher-lying electronic states in the valence band of the mixed spinel. Continuing extraction of Mg^{2+} beyond $x = 0.5$ results in a linearly increasing change of average Bader charge on Cr ions reaching 2.00e at $x = 0$, which is similar to 2.01e charge calculated for a Cr_2O_4 structure[17] with a formal oxidation state of Cr^{4+}. While the spinel Cr_2O_4 was predicted previously, the actual formation and/or the stability of Cr^{4+} in the spinel structure is uncertain due to potential disproportionation into Cr^{3+} and Cr^{6+}. Therefore, we suggest on the basis of Bader charge analysis, that Mn^{3+}/Mn^{4+} redox is dominant in charge and discharge processes at $x > 0.5$ in this mixed spinel composition.

Mn K-edge X-ray absorption spectroscopy (XAS) was employed to understand the element-specific evolution of the electronic environment as a response to the Mg^{2+} reaction (Figure 3b–d). The absorption edge involves a bound state electronic transition from an occupied 1s level to empty valence 3p bands of Mn.[12] The energy position of near-edge features is particularly sensitive to changes in shielding of core electron binding energy by valence electrons, which tracks the formal oxidation state of the metals in the bulk. Figure 3b represented normalized X-ray absorption near edge structure (XANES) region for pristine, charged, and discharged $MgCrMnO_4$ electrodes prepared in a half-cell (Figure 2a). Four standards of Mn-spinel oxides, Mn_3O_4 (Mn^{2+}, Mn^{3+}), $MgMn_2O_4$ (Mn^{3+}), $LiMn_2O_4$ (Mn^{3+}, Mn^{4+}), and Mn_2O_4 (Mn^{4+}), were measured to predict the oxidation state of the ensemble average within each electrode (Figure S13). The energy threshold, E_0, of each spectrum was estimated from points taken at the onset of the mainline, at $0.2 \leq \mu \leq 0.8$ (Figure 3c). The values of the standards showed a linear correlation between the energy threshold and the formal valence state. Following the comparison, the threshold E_0 of the Mn K-edge in the pristine electrode was consistent with the $MgMn_2O_4$ (Mn^{3+}) standard. The anodic reaction induced a shift of ~0.6 eV in the absorption edge toward the lower energy, indicating bulk oxidation of Mn (Figure 3b,c). Upon applying a cathodic current, the absorption edge was shifted back to a position below than the pristine, denoting an over-reduction of Mn, consistent with the X-ray diffraction and microscopic analyses. Distinct levels of over-reduced Mn state between the bulk and surface of the oxide were identified by measuring Mn L-edge spectra collected in a total electron yielding mode, which is sensitive to ~5 nm depth of surface information (Figure S14).[34] The pristine spectra presented intense absorption features at ~639.8, ~ 641.7, and ~642.9 eV, which can be associated with the expected coexistence of Mn^{2+}, Mn^{3+}, and Mn^{4+}. Comparison with spinel Mn_3O_4 (Figure S14b), it revealed a higher intensity at ~641 eV, indicative of a higher ratio of Mn^{3+} in the valences.[34] Upon remagnesiation, a dominant Mn^{2+} at ~639.9 eV was detected, indicating a formation of rock-salt on the surface which was consistent with microscopic analysis (Figure 2d).[34] However, a smaller shift of ~0.1 eV to higher energy in the main edge of Cr K-edge spectra was observed upon demagnesiation (Figure S15). Since the electrochemical potential for oxidation was never reached to the predicted potential of $Cr^{3+/4+}$,[16,17] the changes in valence states of Cr could be explained by the delocalized electrons at the oxidized Mn valence in the Cr–Mn mixed lattices or/and the enhanced kinetics of Mg^{2+} coordinated to Cr by the raised cell temperature.[18] The position of the main edge in the oxidized Cr was reverted to the original position upon reintercalation of Mg^{2+}, a reduction of Cr. Reversible changes for metal redox centers supported a bulk Mg^{2+} activity throughout the designed lattice which are consistent with the

https://dx.doi.org/10.1021/acs.chemmater.0c01988
Chem. Mater. 2020, 32, 6577–6587

trends observed in the X-ray diffraction and microscopic analyses. Information on local coordination at Mn and Cr in the mixed spinel was extracted by an extended X-ray absorption fine structure (EXAFS) technique (Figure 3d). The magnitude of first coordination corresponding to the average Mn−O bonds, was notably increased, whereas the second coordination due to Mn−Mn bonds showed no significant changes upon demagnesiation (Figure 3d). The changes could be explained by the oxidation of Jahn−Teller active Mn^{3+}, which reduced the locally geometric distortion surrounding the Mn ions. Comparison with EXAFS of the Mn standards (Figure S16) also shows a similar trend for the transition from tetragonal $MgMn_2O_4$ to cubic Mn_2O_4. Reintercalation of Mg^{2+} into the oxidized state induced a decrease of intensities in both coordination shells (Figure 3d). The presence of Mn^{2+}, after over-remagnesiation, likely led to the overall increase of local disorder in the spinel lattice. As shown in Figure S17, the changes in Cr coordination were relatively small along with the shift of the main edge, but systematic decreases of magnitudes in both Cr−O and Cr−Cr were observed after the removal of Mg^{2+}. The subtle changes could be due to changes in bonding near neighboring Mn sites in the spinel, and/or slightly oxidized Cr valences. In summary, the electronic structures of Cr and Mn were found to systematically support bulk Mg^{2+} activity throughout the lattice.

Figure 4a represents the theoretical estimation of average potentials, as a function of Mg^{2+} content in the Cr−Mn spinel oxide calculated using the lowest formation energies at different states of charge (Figure S18).[17] The average potential for the anodic reaction was ∼2.8 V (vs Mg/Mg^{2+}) at a relatively constant, up to the composition where half of Mg^{2+} was deintercalated by utilizing Mn redox as predicted in Bader charge analysis (Figure 3a). The predicted potentials raise to above ∼3.6 V (vs Mg/Mg^{2+}) when more than a half of Mg^{2+} deintercalated, upon initializing Cr redox (Figure 4a). The results supported our assumption that Mn is the main redox-participating metal in the Cr−Mn spinel lattice as observed in the spectroscopic analysis. The reaction potentials of the cell paired with carbon capacitance (a half-cell) were converted to the potentials versus Mg/Mg^{2+} by assembling a full-cell conjugated with a Mg metal anode while other conditions of measurement were identical (Figure S19). Similar shapes of anodic reaction were observed in both electrochemical systems, whereas it showed a potential difference of roughly 2.05 V between the cells (Figure S19c,d). This value was used to calibrate the potentials of a half-cell throughout this manuscript. The nanocrystalline $MgCrMnO_4$ was tested in a full-cell, paired with a Mg foil anode at 95 °C at a rate of C/50 (Figure 4b). The anodic potential for demagnesiation showed a plateau at ∼2.9 V (vs Mg/Mg^{2+}), similar to the estimation from DFT calculation. Upon the cathodic reaction, overpotentials comparable to the curves of a half-cell at 95 °C, were observed while two inflection points of potentials were presented at ∼2.4 V and ∼1.5 V (vs Mg/Mg^{2+}). The polarization could be explained by the multifaceted issues including sluggish Mg^{2+}, poor desolvation of Mg^{2+} at the interfaces, and formation of blocking layers on the electrodes.[16,18,26]

One possible strategy to enhance sluggish Mg^{2+} mobility in this system is the reduction of Mg/Mn antisite disorder, which is shown to affect Mg^{2+} ionic mobility in spinel.[16] An attempt to reduce the ratio of inversion in Mg/Mn sites was made by postannealing the pristine powder at 350 °C (post-$MgCrMnO_4$), where an exothermic reaction takes place, captured by thermal gravimetric analysis (Figure S20).[14,16] As shown in Figure S21, the refinement of post-$MgCrMnO_4$ indicated a decreased ratio of inversion ($\lambda \approx 0.1$) without any segregated new phases, in turn recruiting more extractable lattice Mg^{2+} along with lowered activation barriers for cation migration.[13,16] The post-$MgCrMnO_4$ cell at 25 °C presented an enhancement of capacities in both anodic and cathodic reactions within the same potential window compared to the pristine (Figure S22a). However, a decrease of Mg^{2+} (de)-intercalation at room temperature was observed upon the subsequent cycle due to possibly a sluggish behavior of Mg^{2+} migration, desolvation barriers in the electrode/electrolyte interfaces and/or a lack of conductive nature of SEI on the electrode which require further focus in the future (Figure S23). At the raised temperature (95 °C) as shown in Figure S22b, the extent of polarization was reduced remarkably while obtaining an extended capacity at the potential of ∼0.4 V (vs carbon), which could be converted to ∼2.4 V (vs Mg/Mg^{2+}). It is intriguing that the enhancement is solely correlated to the reduced degree of antisite disorder since no other structural or morphological parameters are changed after the postannealing.[13,16] The kinetics of the electrochemical reaction at various temperatures, another factor for lowering migration barriers in bulk and at interfaces, were investigated by operating the post-$MgCrMnO_4$ electrode half-cells at 25, 60, and 95 °C (Figure 4c). The anodic potentials for demagnesiation were steadily lowered with increasing cell temperatures, which is ascribed to be improved Mg^{2+} kinetics. Upon remagnesiation, the cathodic curves of the cells, especially at 60 and 95 °C, revealed relatively higher potentials for reduction which corresponds to a dramatic increase in harvested energy density from the material. Simply put, modification of structural complexity enhances utilizable lattice Mg^{2+} and energy in the oxide frame. The cell at 60 °C which provides moderate Mg^{2+} activity along with less decomposition of the electrolyte, was cycled within the potentials between −1.2 and 1.2 V (Figure 4d), which could be approximately converted to a 3.2−0.8 V (vs Mg/Mg^{2+}). The cell was galvanostatically charged up to 1.2 V (vs carbon) at a rate of C/50 where ∼125 mAh/g of capacity was delivered (Figure 4d). On the subsequent discharging, a capacity of ∼75 mAh/g with an average voltage of ∼2.4 V (vs Mg/Mg^{2+}) was achieved by −1.2 V (vs carbon) corresponding to ∼180 Wh/kg of energy density, which was close to the values (200−250 Wh/kg) of the current Li-ion battery technology (Figure S24). While the reversible capacity steadily drops in the following cycles, a discharge capacity of 44 mAh/g and 23 mAh/g were delivered at cycle No. 2 and 50, respectively.

The electrode after 50 cycles was analyzed by X-ray diffraction to track any formation of secondary phases produced by undesired reaction pathways, such as conversion (Figure S25). No visible secondary phases were detected whereas two distinct spinel structures larger than the pristine were found via Rietveld refinement analysis. The expanded lattices, very similar to the observed values for remagnesiated larger particles, can again be explained by overmagnesiation at 16d sites, and/or increase of inversion in repeated cycles. While the origin of this interesting reversible phenomenon is not clear as of now, but it will be explored in a follow-up detailed structural study. The electrochemical results consistently agree with both experimental and theoretical analyses, revealing the mechanism of Mg^{2+} (de)-intercalation within the spinel lattice where strong electrostatic interaction exists. Overall outcomes of this study showed promise to approach a functional Mg-ion spinel oxide cathode

https://dx.doi.org/10.1021/acs.chemmater.0c01988
Chem. Mater. 2020, 32, 6577−6587

operated at high potentials at moderate temperatures by electrochemical Mg^{2+} intercalation. All in all, the study provides a pathway for design rules to enhance lattice Mg^{2+} activity, suggesting the next direction of exploring the oxide spinels.

CONCLUSIONS

In this work, the capability of the tailored $MgCrMnO_4$ spinel to (de)intercalate Mg^{2+} electrochemically at high potentials was evaluated by the theoretical and experimental approaches. High Mg^{2+} activity was observed in bulk, with a remarkable degree of lattice breathing and reversibility. Characterization of key electrochemical states through a combination of X-ray absorption spectroscopy, nuclear magnetic resonance spectroscopy, electron microscopy, density functional theory calculation, and X-ray diffraction revealed structural, compositional, and redox changes, consistent with a reaction mechanism through the (de)intercalation of Mg^{2+}. A potential plateau at roughly 3.0 V (vs Mg/Mg^{2+}) for oxidation was shown at a raised temperature of electrochemical reaction (95 °C), consistent with the theoretical estimates. Notable level of reversible Mg^{2+} intercalation was observed, albeit with significant overpotential. We show that it could be mitigated dramatically by reducing the ratio of Mg/Mn inversion in the lattice by postannealing the spinel at 350 °C, enhancing the Mg^{2+} mobility in the lattice. Possible cyclability at moderate temperature (60 °C) was observed along with a ∼180 Wh/kg of energy density delivered at the first discharge reaction. This study redefines lattice design via chemical and structural composition of functional spinel oxides utilized by Mg^{2+} intercalation at high potentials. Our findings uncover a new subclass of cathode material for rechargeable Mg-ion batteries.

METHODS

Synthesis. $MgCrMnO_4$, $MgMn_2O_4$, and $MgCr_2O_4$ were synthesized by an aqueous sol−gel reaction, followed by annealing at various temperatures. Magnesium acetate tetrahydrate ($Mg(CH_3COO)_2 \cdot 4H_2O$, Product No. M5661 in Sigma-Aldrich), chromium acetate hydroxide ($Cr_3(CH_3CO_2)_7(OH)_2$, Product No. 318108 in Sigma-Aldrich), manganese acetate dihydrate ($Mn(CH_3COO)_3 \cdot 4H_2O$, Product No. 215880 in Sigma-Aldrich) were used as a precursor, and citric acid ($C_6H_8O_7$, Product No. C0759 in Sigma-Aldrich) was introduced as a capping agent. 12.5 mmol of precursors and 25.0 mmol of citric acid were dissolved in 200 mL of deionized water and it was stirred vigorously for 30 min. The mixture was then heated at 120 °C to evaporate water until the powder was obtained. The powders were calcined in air at the temperatures (700 and 950 °C), depending on the purpose of synthesis. Post-$MgCrMnO_4$ was obtained by postannealing the pristine oxides at 350 °C in air for 24 h. Standard $MgMn_2O_4$ was synthesized by calcining the precursor at 950 °C for 24 h in air then it was postannealed at 400 °C for 72 h, followed by a quench at room temperature.[16] $MgCr_2O_4$ was prepared by calcining the precursor at 950 °C for 24 h in air.

Modelings and Characterizations. Theoretical values of the average cell potentials and Mg migration barriers of $MgCrMnO_4$ were obtained from density functional theory calculations as implemented in Vienna Ab initio Simulation Package (VASP).[35] The core−valence electron interactions were treated using the projector-augmented wave (PAW) potentials.[36] The exchange-correlation functionals were described by the generalized gradient approximation (GGA) method developed by Perdew−Burke−Ernzerhof (PBE).[37] A Hubbard U correction was also added to describe the localization of d-electrons of redox-active species, Cr (U = 3.7 eV) and Mn (U = 3.9 eV).[38] The average cell potential was calculated from the energy difference between the charged and discharged phases. The Mg migration barriers are calculated by the nudged elastic band method (NEB) method, where a 2 × 2 × 2 supercell of the primitive cell was used to avoid fictitious interactions between periodic images of diffusing atoms.[39] The distribution of Cr and Mn atoms in the spinel structure was chosen using the Pymatgen code to minimize the electrostatic energy of the cell. The NEB calculations are performed with GGA functional without U correction as suggested in reference.[8]

High-resolution synchrotron X-ray diffraction data were collected at 11-BM beamline at the Advanced Photon Source (APS), Argonne National Laboratory (ANL) (λ = 0.412794, 0.412834, 0.412818, 0.412828, and 0.457841 Å). Samples were loaded in Kapton capillaries and mounted on bases provided by the APS. Structures were refined using the Rietveld method as implemented in the TOPAS software package (Bruker-AXS, version 6) across a d-spacing range of 5.0 Å to 0.5 Å. Full Width Half Maximum (fwhm) and Integral Breath (IB) based on volume-weighted column heights (LVol) were estimated by the macro function of "LVol FWHM CS G L" in TOPAS.

Atomic-resolution annular dark field and bright field imaging, as well as EELS and EDX spectroscopies, were performed on an aberration-corrected JEOL JEM-ARM200CF operated at 200 kV which can achieve a spatial resolution of ∼73 pm. The ARM200CF is equipped with a cold-field emission gun, providing an energy resolution of 350 meV, as well as an Oxford X-Max 100TLE windowless silicon drift EDX detector. Images were acquired using high-angle annular dark-field (HAADF) imaging, where the resulting image contrast is proportional to Z^2, low angle annular dark field (LAADF) imaging, which is sensitive to strain contrast and incoherent annular bright-field (ABF) imaging, which is sensitive to light elements.

Solid-state ^{25}Mg magic angle spinning (MAS) NMR experiments were performed at 11.7 T (500 MHz) on a Bruker Avance III spectrometer operating at a Larmor frequency of 30.64 MHz using a 3.2 mm MAS probe. The spectra were acquired at a spinning speed of 20 kHz using 3.2 mm rotors with a rotor synchronized spin−echo experiment (90°−τ−180°−τ) where τ is 1/r. To ensure quantification in normalized intensity plots, single pulse experiments (data not shown) with recycle delays 0.1 to 1 s were used to confirm signal saturation. All ^{25}Mg shifts were referenced to 5 M $MgCl_2$ (aq.) at 0 ppm.

The electrochemical performance was evaluated on composites containing the $MgCrMnO_4$ as working electrodes. Electrode slurries were prepared by mixing the active material, Timcal C45 carbon, and 6 wt % of a binder solution consisting of polyvinylidene difluoride (PVDF, Solvay) in N-methylpyrrolidone (NMP, Sigma-Aldrich) to produce a dry electrode with a 6:2:2 ratio. Then, the slurry was cast on a stainless-steel foil, and it was dried under vacuum at 80 °C to evaporate NMP. The loading level of active oxide in the dry electrodes was adapted to around 4−6 mg/cm^2. Circular pieces with a diameter of 3/8 in. were punched and assembled in two-electrode coin cells in a glovebox filled with inert Ar gas where the levels of water and oxygen contents were ≤1.0 ppm. Half-cell measurements were conducted in 0.1 M $Mg[TPFA]_2$ ($[TPFA]^- = [(Al(OC(CF_3)_3)_4)^-]$) dissolved in triglyme.[19] The counter electrode was activated carbon, which was prepared by mixing activated carbon, Timcal C45 carbon, and PVDF with a ratio of 8:1:1 (wt%). The high specific surface area of the activated carbon gives rise to sufficient double-layer charging to match the charge needed to cycle the cathode.[40] Full-cells paired with a magnesium foil (purity 99.9%, Sigma-Aldrich) were built using 0.1 M $Mg[TPFA]_2$/triglyme electrolyte. Glass microfiber filters (VWR 28297−289) were used as separators in the coin cell experiment. Electrochemical measurements were performed on a MACCOR battery cycler at 25, 60, and 95 °C. The potentials in this report are referenced to the activated carbon or Mg/Mg^{2+} couple depending on the cell configuration. The rate, C/n, was defined as the current density required to achieve a theoretical capacity of $MgCrMnO_4$, C = 280 mAh/g, in n hours, assuming the reaction of $MgCrMnO_4 \leftrightarrow Mg^{2+} + CrMnO_4$. Electrodes harvested for further characterization were washed multiple times with acetonitrile to remove electrolyte residues.

Thermal gravimetric analysis was carried out with a SDT-Q600 (TA Instruments) in the temperature ranged from 50 to 800 °C at a heating rate of 3 °C/min under synthetic air.

Mn K-edge X-ray absorption near-edge structure (XANES) was performed at the MRCAT bending magnet beamline 10 μ_B at the

https://dx.doi.org/10.1021/acs.chemmater.0c01988
Chem. Mater. 2020, 32, 6577−6587

Advanced Photon Source, Argonne National Laboratory (ANL). X-ray absorption spectra were collected in a transmission mode through the electrochemically treated ex-situ electrodes. Energy was scanned by a double-crystal Si (111) monochromator that was detuned by 50% and the incident and transmitted intensity was measured by gas ionization chambers. Mn and Cr metal reference foil were measured simultaneously with each sample for energy calibration. Data analysis was completed using the IFEFFIT package. Mn $L_{II, III}$-edge X-ray absorption spectroscopy (XAS) measurements were carried out beamline 4-ID-C at Advanced Photon Source (APS) at Argonne National Laboratory (ANL, Lemont, IL). To verify the electronic environment on the surface of the oxides, the Mn L-edge spectra were collected in a total electron yield (TEY) mode at room temperature and under ultrahigh vacuum conditions (below 10^{-8} Torr). Contributions from visible light were carefully minimized before the acquisition, and all spectra were normalized by the current from freshly evaporated gold on a fine grid positioned upstream of the main chamber. The measured spectra were aligned by the beamline reference and a basic normalization using a linear background. Standard spinel oxides, Mn_3O_4 and $LiMn_2O_4$ (Sigma-Aldrich), were used as-received from a commercial supplier. The Mn_2O_4 spinel was prepared by electrochemical delithiation of $LiMn_2O_4$ (charge to 4.3 V vs Li/Li^+) in Gen 2 electrolyte paired with a Li foil.[30]

■ ASSOCIATED CONTENT

Supporting Information

The Supporting Information is available free of charge at https://pubs.acs.org/doi/10.1021/acs.chemmater.0c01988.

Minimum energy pathways of Mg^{2+} in $MgCr_2O_4$; EDX spectra of pristine $MgCrMnO_4$; particle size distribution of $MgCrMnO_4$ nanocrystals; HAADF images of $MgCrMnO_4$; SEM-EDX of charged $MgCrMnO_4$; synchrotron XRD patterns of ex-situ electrodes; potential versus capacity profiles of $MgCrMnO_4$; corresponding XRD patterns, particle size distribution; potential versus capacity profiles of $MgCrMnO_4$ synthesized at 950 °C; synchrotron XRD patterns of the ex-situ electrodes; schematic description of the proposed mechanism; LAADF images and EELS spectra of pristine and charged $MgCrMnO_4$; EDX mapping of discharged $MgCrMnO_4$; Mn K-edge spectra of Mn spinel standards; Mn L-edge spectra of pristine and discharged $MgCrMnO_4$ electrodes; Cr K-edge spectra; Mn K-edge extended X-ray absorption fine structure of standard Mn spinels; Cr K-edge extended X-ray absorption fine structure of $MgCrMnO_4$; ground state hull of Mg_xCrMnO_4 system; potential versus capacity profiles of $MgCrMnO_4$ in a half- and full-cell; thermal gravimetric analysis of pristine $MgCrMnO_4$; synchrotron XRD Rietveld refinement of post-$MgCrMnO_4$; potential versus capacity profiles of $MgCrMnO_4$ and post-$MgCrMnO_4$ at various temperatures; potential versus capacity profiles of post-$MgCrMnO_4$ at first and second cycle; an incremental capacity plot of cathodic reaction in post-$MgCrMnO_4$ electrode; and synchrotron XRD pattern of the electrode after 50 cycles (PDF)

■ AUTHOR INFORMATION

Corresponding Authors

Bob Jin Kwon − *Chemical Sciences and Engineering Division and Joint Center for Energy Storage Research, Argonne National Laboratory, Lemont, Illinois 60439, United States;* orcid.org/0000-0001-7395-0814; Email: bkwon@anl.gov

Baris Key − *Chemical Sciences and Engineering Division and Joint Center for Energy Storage Research, Argonne National Laboratory, Lemont, Illinois 60439, United States;* orcid.org/0000-0002-1987-1629; Email: bkey@anl.gov

Authors

Liang Yin − *Joint Center for Energy Storage Research and X-ray Science Division, Advanced Photon Source, Argonne National Laboratory, Lemont, Illinois 60439, United States;* orcid.org/0000-0001-5396-782X

Haesun Park − *Joint Center for Energy Storage Research and Materials Science Division, Argonne National Laboratory, Lemont, Illinois 60439, United States;* orcid.org/0000-0001-6266-8151

Prakash Parajuli − *Joint Center for Energy Storage Research, Argonne National Laboratory, Lemont, Illinois 60439, United States; Department of Physics, University of Illinois at Chicago, Chicago, Illinois 60607, United States*

Khagesh Kumar − *Joint Center for Energy Storage Research, Argonne National Laboratory, Lemont, Illinois 60439, United States; Department of Chemistry, University of Illinois at Chicago, Chicago, Illinois 60607, United States*

Sanghyeon Kim − *Chemical Sciences and Engineering Division and Joint Center for Energy Storage Research, Argonne National Laboratory, Lemont, Illinois 60439, United States*

Mengxi Yang − *Chemical Sciences and Engineering Division and Joint Center for Energy Storage Research, Argonne National Laboratory, Lemont, Illinois 60439, United States*

Megan Murphy − *Joint Center for Energy Storage Research, Argonne National Laboratory, Lemont, Illinois 60439, United States; Department of Chemistry, University of Illinois at Chicago, Chicago, Illinois 60607, United States*

Peter Zapol − *Joint Center for Energy Storage Research and Materials Science Division, Argonne National Laboratory, Lemont, Illinois 60439, United States;* orcid.org/0000-0003-0570-9169

Chen Liao − *Chemical Sciences and Engineering Division and Joint Center for Energy Storage Research, Argonne National Laboratory, Lemont, Illinois 60439, United States;* orcid.org/0000-0001-5168-6493

Timothy T. Fister − *Chemical Sciences and Engineering Division and Joint Center for Energy Storage Research, Argonne National Laboratory, Lemont, Illinois 60439, United States;* orcid.org/0000-0001-6537-6170

Robert F. Klie − *Joint Center for Energy Storage Research, Argonne National Laboratory, Lemont, Illinois 60439, United States; Department of Physics, University of Illinois at Chicago, Chicago, Illinois 60607, United States;* orcid.org/0000-0003-4773-6667

Jordi Cabana − *Joint Center for Energy Storage Research, Argonne National Laboratory, Lemont, Illinois 60439, United States; Department of Chemistry, University of Illinois at Chicago, Chicago, Illinois 60607, United States;* orcid.org/0000-0002-2353-5986

John T. Vaughey − *Chemical Sciences and Engineering Division and Joint Center for Energy Storage Research, Argonne National Laboratory, Lemont, Illinois 60439, United States;* orcid.org/0000-0002-2556-6129

Saul H. Lapidus − *Joint Center for Energy Storage Research and X-ray Science Division, Advanced Photon Source, Argonne National Laboratory, Lemont, Illinois 60439, United States*

Complete contact information is available at: https://pubs.acs.org/10.1021/acs.chemmater.0c01988

https://dx.doi.org/10.1021/acs.chemmater.0c01988
Chem. Mater. 2020, 32, 6577−6587

Author Contributions

B.J.K., J.T.V., and B.K. designed this project. B.J.K. synthesized the samples. L.Y. and S.H.L. collected diffraction and performed the structural characterization. B.J.K. and S.K. performed electrochemical experiments. P.P. and R.F.K. collected electron microscopic data. H.P. and P.Z. performed theoretical calculations. K.K., M.M., T.T.F., and J.C. performed X-ray absorption spectroscopy. M.Y. and C.L. synthesized the Mg electrolyte. B.J.K., L.Y., and B.K. wrote the manuscript, following which all authors approved the final version.

Notes

The authors declare no competing financial interest.

■ ACKNOWLEDGMENTS

This work is solely supported by the Joint Center for Energy Storage Research (JCESR) and Energy Innovation Hub funded by the U.S. Department of Energy (DOE), Office of Science, Basic Energy Sciences. The acquisition of the UIC JEOL JEM ARM200CF was supported by an MRI-R^2 grant from the National Science Foundation (Grant No. DMR-0959470) and the upgraded Gatan Continuum spectrometer was supported by a grant from the NSF (DMR-1626065). This work made use of instruments in the Electron Microscopy Service at the Research Resources Center at UIC. Department of Energy (DOE) Office of Science user facility operated for the DOE Office of Science by Argonne National Laboratory under contract no. DE-AC02-06CH11357. Use of the Advanced Photon Source at Argonne National Laboratory was supported by the U.S. Department of Energy, Office of Science, Office of Basic Energy Sciences, under Contract No. DE-AC02-06CH11357.

■ REFERENCES

(1) Levi, E.; Gofer, Y.; Aurbach, D. On the Way to Rechargeable Mg Batteries: The Challenge of New Cathode Materials. *Chem. Mater.* **2010**, *22* (3), 860−868.

(2) Muldoon, J.; Bucur, C. B.; Gregory, T. Quest for Nonaqueous Multivalent Secondary Batteries: Magnesium and Beyond. *Chem. Rev.* **2014**, *114* (23), 11683−11720.

(3) Mao, M. L.; Gao, T.; Hou, S. Y.; Wang, C. S. A critical review of cathodes for rechargeable Mg batteries. *Chem. Soc. Rev.* **2018**, *47* (23), 8804−8841.

(4) Song, J.; Sahadeo, E.; Noked, M.; Lee, S. B. Mapping the Challenges of Magnesium Battery. *J. Phys. Chem. Lett.* **2016**, *7* (9), 1736−1749.

(5) Sun, X. Q.; Bonnick, P.; Duffort, V.; Liu, M.; Rong, Z. Q.; Persson, K. A.; Ceder, G.; Nazar, L. F. A high capacity thiospinel cathode for Mg batteries. *Energy Environ. Sci.* **2016**, *9* (7), 2273−2277.

(6) Aurbach, D.; Lu, Z.; Schechter, A.; Gofer, Y.; Gizbar, H.; Turgeman, R.; Cohen, Y.; Moshkovich, M.; Levi, E. Prototype systems for rechargeable magnesium batteries. *Nature* **2000**, *407* (6805), 724−727.

(7) Hannah, D. C.; Gautam, G. S.; Canepa, P.; Ceder, G., On the Balance of Intercalation and Conversion Reactions in Battery Cathodes. *Adv. Energy. Mater.* **2018**, *8* (20), 1800379.

(8) Liu, M.; Rong, Z. Q.; Malik, R.; Canepa, P.; Jain, A.; Ceder, G.; Persson, K. A. Spinel compounds as multivalent battery cathodes: a systematic evaluation based on ab initio calculations. *Energy Environ. Sci.* **2015**, *8* (3), 964−974.

(9) Sun, X. Q.; Duffort, V.; Mehdi, B. L.; Browning, N. D.; Nazar, L. F. Investigation of the Mechanism of Mg Insertion in Birnessite in Nonaqueous and Aqueous Rechargeable Mg-Ion Batteries. *Chem. Mater.* **2016**, *28* (2), 534−542.

(10) Arthur, T. S.; Zhang, R. G.; Ling, C.; Glans, P. A.; Fan, X. D.; Guo, J. H.; Mizuno, F. Understanding the Electrochemical Mechanism of K-alpha MnO_2 for Magnesium Battery Cathodes. *ACS Appl. Mater. Interfaces* **2014**, *6* (10), 7004−7008.

(11) Rong, Z. Q.; Malik, R.; Canepa, P.; Gautam, G. S.; Liu, M.; Jain, A.; Persson, K.; Ceder, G. Materials Design Rules for Multivalent Ion Mobility in Intercalation Structures. *Chem. Mater.* **2015**, *27* (17), 6016−6021.

(12) Kim, C.; Phillips, P. J.; Key, B.; Yi, T. H.; Nordlund, D.; Yu, Y. S.; Bayliss, R. D.; Han, S. D.; He, M. N.; Zhang, Z. C.; Burrell, A. K.; Klie, R. F.; Cabana, J. Direct Observation of Reversible Magnesium Ion Intercalation into a Spinel Oxide Host. *Adv. Mater.* **2015**, *27* (22), 3377−3384.

(13) Gautam, G. S.; Canepa, P.; Urban, A.; Bo, S. H.; Ceder, G. Influence of Inversion on Mg Mobility and Electrochemistry in Spinels. *Chem. Mater.* **2017**, *29* (18), 7918−7930.

(14) Zhang, X. W.; Zunger, A. Diagrammatic Separation of Different Crystal Structures of A(2)BX(4) Compounds Without Energy Minimization: A Pseudopotential Orbital Radii Approach. *Adv. Funct. Mater.* **2010**, *20* (12), 1944−1952.

(15) Radhakrishnan, N. K.; Biswas, A. B. Cation Distribution in Tetragonal Spinel $MgMn_2O_4$. *Z. Kristallogr. - Cryst. Mater.* **1975**, *142* (1−2), 117−120.

(16) Bayliss, R. D.; Key, B.; Sai Gautam, G.; Canepa, P.; Kwon, B. J.; Lapidus, S. H.; Dogan, F.; Adil, A. A.; Lipton, A. S.; Baker, P. J.; et al. Probing Mg Migration in Spinel Oxides. *Chem. Mater.* **2020**, *32* (2), 663−670.

(17) Chen, T. N.; Gautam, G. S.; Huang, W. X.; Ceder, G. First-Principles Study of the Voltage Profile and Mobility of Mg Intercalation in a Chromium Oxide Spinel. *Chem. Mater.* **2018**, *30* (1), 153−162.

(18) Kwon, B. J.; Lau, K.-C.; Park, H.; Wu, Y. A.; Hawthorne, K. L.; Li, H.; Kim, S.; Bolotin, I. L.; Fister, T. T.; Zapol, P.; et al. Probing Electrochemical Mg-Ion Activity in $MgCr_{2-x}V_xO_4$ Spinel Oxides. *Chem. Mater.* **2020**, *32* (3), 1162−1171.

(19) Lau, K. C.; Seguin, T. J.; Carino, E. V.; Hahn, N. T.; Connell, J. G.; Ingram, B. J.; Persson, K. A.; Zavadil, K. R.; Liao, C. Widening Electrochemical Window of Mg Salt by Weakly Coordinating Perfluoroalkoxyaluminate Anion for Mg Battery Electrolyte. *J. Electrochem. Soc.* **2019**, *166* (8), A1510−A1519.

(20) Golikov, Y. V.; Barkhatov, V. P.; Balakirev, V. F.; Chufarov, G. I. Thermal-Dissociation and Reduction of $MgMn_2O_4$. *Zh Fiz Khim+* **1982**, *56* (12), 2965−2967.

(21) Stefan, E.; Connor, P. A.; Azad, A. K.; Irvine, J. T. S. Structure and properties of $MgM_xCr_{2-x}O_4$ (M = Li, Mg, Ti, Fe, Cu, Ga) spinels for electrode supports in solid oxide fuel cells. *J. Mater. Chem. A* **2014**, *2* (42), 18106−18114.

(22) West, A. R. *Solid State Chemistry and its Applications*; John Wiley & Sons, 2014.

(23) Radhakrishnan, N. K.; Biswas, A. B. Neutron-Diffraction Study of Cation Migration in $MgMn_2O_4$. *Phys. Status Solidi A* **1976**, *37* (2), 719.

(24) Lee, J.; Seymour, L. D.; Pell, A. J.; Dutton, S. E.; Grey, C. P. A systematic study of Mg-25 NMR in paramagnetic transition metal oxides: applications to Mg-ion battery materials. *Phys. Chem. Chem. Phys.* **2017**, *19* (1), 613−625.

(25) Zeng, D. L.; Cabana, J.; Breger, J. L.; Yoon, W. S.; Grey, C. P. Cation ordering in $Li[Ni_xMn_xCo_{(1-2x)}]O_2$-layered cathode materials: A nuclear magnetic resonance (NMR), pair distribution function, X-ray absorption spectroscopy, and electrochemical study. *Chem. Mater.* **2007**, *19* (25), 6277−6289.

(26) Wang, H.; Senguttuvan, P.; Proffit, D. L.; Pan, B. F.; Liao, C.; Burrell, A. K.; Vaughey, J. T.; Key, B. Formation of MgO during Chemical Magnesiation of Mg-Ion Battery Materials. *ECS Electrochem. Lett.* **2015**, *4* (8), A90.

(27) Ruch, P. W.; Cericola, D.; Hahn, M.; Kotz, R.; Wokaun, A. On the use of activated carbon as a quasi-reference electrode in non-aqueous electrolyte solutions. *J. Electroanal. Chem.* **2009**, *636* (1−2), 128−131.

(28) Nam, K. W.; Kim, S.; Lee, S.; Salama, M.; Shterenberg, I.; Gofer, Y.; Kim, J. S.; Yang, E.; Park, C. S.; Kim, J. S.; Lee, S. S.; Chang, W. S.; Doo, S. G.; Jo, Y. N.; Jung, Y.; Aurbach, D.; Choi, J. W. The High Performance of Crystal Water Containing Manganese Birnessite

https://dx.doi.org/10.1021/acs.chemmater.0c01988
Chem. Mater. 2020, 32, 6577−6587

Cathodes for Magnesium Batteries. *Nano Lett.* **2015**, *15* (6), 4071−4079.
(29) Truong, Q. D.; Devaraju, M. K.; Tran, P. D.; Gambe, Y.; Nayuki, K.; Sasaki, Y.; Honma, I. Unravelling the Surface Structure of $MgMn_2O_4$ Cathode Materials for Rechargeable Magnesium-Ion Battery. *Chem. Mater.* **2017**, *29* (15), 6245−6251.
(30) Kwon, B. J.; Dogan, F.; Jokisaari, J. R.; Key, B.; Kim, C.; Liu, Y. S.; Guo, J. H.; Klie, R. F.; Cabana, J. Effect of Passivating Shells on the Chemistry and Electrode Properties of $LiMn_2O_4$ Nanocrystal Heterostructures. *ACS Appl. Mater. Interfaces* **2019**, *11* (4), 3823−3833.
(31) Kim, C.; Adil, A. A.; Bayliss, R. D.; Kinnibrugh, T. L.; Lapidus, S. H.; Nolis, G. M.; Freeland, J. W.; Phillips, P. J.; Yi, T. H.; Yoo, H. D.; Kwon, B. J.; Yu, Y. S.; Klie, R.; Chupas, P. J.; Chapman, K. W.; Cabana, J. Multivalent Electrochemistry of Spinel $Mg_xMn_{3-x}O_4$ Nanocrystals. *Chem. Mater.* **2018**, *30* (5), 1496−1504.
(32) Shimokawa, K.; Atsumi, T.; Harada, M.; Ward, R. E.; Nakayama, M.; Kumagai, Y.; Oba, F.; Okamoto, N. L.; Kanamura, K.; Ichitsubo, T. Zinc-based spinel cathode materials for magnesium rechargeable batteries: toward the reversible spinel-rocksalt transition. *J. Mater. Chem. A* **2019**, *7* (19), 12225−12235.
(33) Tang, W.; Sanville, E.; Henkelman, G. E Henkelman, G, A grid-based Bader analysis algorithm without lattice bias. *J. Phys.: Condens. Matter* **2009**, *21* (8), 084204.
(34) Nolis, G. M.; Adil, A.; Yoo, H. D.; Hu, L. H.; Bayliss, R. D.; Lapidus, S. H.; Berkland, L.; Phillips, P. J.; Freeland, J. W.; Kim, C.; Klie, R. F.; Cabana, J. Electrochemical Reduction of a Spinel-Type Manganese Oxide Cathode in Aqueous Electrolytes with Ca^{2+} or Zn^{2+}. *J. Phys. Chem. C* **2018**, *122* (8), 4182−4188.
(35) Kresse, G.; Furthmuller, J. Efficient iterative schemes for ab initio total-energy calculations using a plane-wave basis set. *Phys. Rev. B: Condens. Matter Mater. Phys.* **1996**, *54* (16), 11169−11186.
(36) Blochl, P. E. Projector Augmented-Wave Method. *Phys. Rev. B: Condens. Matter Mater. Phys.* **1994**, *50* (24), 17953−17979.
(37) Perdew, J. P.; Burke, K.; Ernzerhof, M. Generalized gradient approximation made simple. *Phys. Rev. Lett.* **1996**, *77* (18), 3865−3868.
(38) Dudarev, S. L.; Botton, G. A.; Savrasov, S. Y.; Humphreys, C. J.; Sutton, A. P. Electron-energy-loss spectra and the structural stability of nickel oxide: An LSDA+U study. *Phys. Rev. B: Condens. Matter Mater. Phys.* **1998**, *57* (3), 1505−1509.
(39) Henkelman, G.; Uberuaga, B. P.; Jónsson, H. A climbing image nudged elastic band method for finding saddle points and minimum energy paths. *J. Chem. Phys.* **2000**, *113* (22), 9901−9904.
(40) Yoo, H. D.; Jokisaari, J. R.; Yu, Y.-S.; Kwon, B. J.; Hu, L.; Kim, S.; Han, S.-D.; Lopez, M.; Lapidus, S. H.; Nolis, G. M.; et al. Intercalation of Magnesium into a Layered Vanadium Oxide with High Capacity. *ACS Energy. Lett.* **2019**, *4* (7), 1528−1534.

https://dx.doi.org/10.1021/acs.chemmater.0c01988
Chem. Mater. 2020, 32, 6577−6587